## SI Appendix

### Pre-Processing of BOLD Signal and the Origin of Anticorrelations

Pre-processing of BOLD data consists of three steps: first, averaging of BOLD signal across voxels within each of the 998 ROIs; second, linear detrending of the signal in consecutive 50-second time-windows for each ROI in turn; third, linear regression of mean global BOLD signal, mean ventricular BOLD signal and mean white matter BOLD signals from each ROI in turn. The residuals obtained from the linear regression are then entered into Pearson correlations for the calculation of rsFC.

We found that the piecewise linear detrending step and nuisance regression step strengthened the SC-rsFC relationships that we report here, and this suggests that they successfully removed noise in BOLD signal due to hemodynamic, cardiac and vascular effects. However, it is known [1] that the regression step can potentially induce artefacts in the rsFC maps.

Suppose we have two normally distributed random variables, A and B, which are statistically independent, and of which we have taken *N* samples. If we regress our samples $A_n$ and $B_n$ on some third data series $C_n$, then the residuals of this regression (Resid-$A_n$ and Resid-$B_n$) will sometimes exhibit a statistical dependence. In particular, if $C_n$ is the mean of $A_n$ and $B_n$ , then Resid-$A_n$ and Resid-$B_n$ will be tend to be anti-correlated. Intuitively, this is because whenever $A_n$ is larger than $B_n$, then $A_n$ will be larger than $C_n$ (i.e. the mean), whereas $B_n$ will be less than $C_n$. Thus, Resid-$A_n$ will be positive when Resid-$B_n$ is negative (and vice versa).

This simple example illustrates a phenomenon that can also occur in far more complicated systems such as the cerebral cortex. Some of the anti-correlations observed in fMRI rsFC maps are therefore likely to be artefactual, and are not representative of genuine anticorrelation in underlying neuronal activity. An additional complication is the fact that the strength of induced correlations and anti-correlations will vary depending on how strongly correlated each ROI is with the various regressors (mean global, ventricular and white-matter BOLD signals), and that this in turn will depend on whether that ROI is a member of a cluster of ROI whose BOLD signals vary coherently. There is evidence [2] that some regions – including those within the DMN – are more correlated with the global mean signal than others, and if this substantially affects the manner in which time series from these regions respond to data pre-processing, then pre-processing could produce a range of confounding influences in subsequent data analysis.

The effects we report in this paper cannot be explained as a result of global mean regression, however. We note that the structure-function relationship depicted in Figure 1A is only slightly weakened when we exclude from the calculation all edges with $FC < 0$ (Fig S3B). We recalculated rsFC without performing global mean regression step, instead regressing out only the mean signals from the white matter and the ventricles, which are

spatially distinct from the ROIs in the gray matter. Using this alternate pre-processing step, we continued to observe anticorrelations in the data and as well as a robust SC-rsFC relationship.

The general pattern of our results (e.g. Fig. 1B) is that stronger SC produces stronger rsFC, and the simplest interpretation of the data is that long-range interactions tend to facilitate correlation rather than anti-correlation. Furthermore, because most anti-correlations are observed between region pairs for which SC is absent (Fig. 1D), we expect that most anti-correlations in rsFC do not reflect inhibition mediated by direct cortico-cortical projections. However, when we examine region pairs that exhibit strong anti-correlation but which do have SC, we observe that one member of the region pair is usually located within the Default Mode Network (DMN). One interpretation of this finding is that the Default Mode Network does engage in long range inhibitory interactions. Another interpretation is that regions in the Default Mode Network are particularly susceptible to the artefacts induced by the regression of global BOLD signal. Further work is necessary to settle this important issue.

**Inter-Participant Differences in SC and rsFC**

In order to test whether individual differences in SC are associated with individual differences in rsFC, we computed all pairwise correlations between the SC and rsFC maps of the 5 participants. Table S2 shows the result of the correlations calculated over all region pairs as well as the results over SC-present region pairs.

Across all ROI pairs, the rsFC of 5 out of 5 participants was most highly correlated with their own SC. The mean SC-rsFC correlation within participants was greater than the mean SC-rsFC correlation across participants, but this difference did not reach significance within our sample of five participants (0.223 versus 0.207, $p = 0.12$, two-sample t-test). When including only SC-present edges, 3 of 5 participant best matched their rsFC with their own SC, and the mean correlation was again slightly greater within participants than across participants (0.425 versus 0.397, $p = 0.06$, two-sample t-test). In low resolution matrices, we did not observe a substantial effect of individual differences.

Because the differences in correlation are relatively small, because of the potential influence of differences in ROI registration, and because of our limited sample size, these results are far from definitive, but they provide some support for the claim that individual differences in SC and in rsFC are indeed related to one another, as predicted in [7].

**Regional Differences in the SC-rsFC Relationship**

We expect that some regions of the brain are more strongly driven by endogenous dynamics, while others are more strongly influenced by the activity of their neighbors.

Those that are more strongly coupled to their neighbors should show a stronger SC-rsFC relationship. In order to investigate regional differences in the strength of the SC-rsFC relationship we calculated SC-rsFC correlations separately for each region at the low resolution. Correlations were computed between single columns of the low resolution SC and rsFC matrices, which correspond to the SC and rsFC of a single anatomical region with all other regions (regardless of whether structural connections are present or not). Correlations as well as SC and rsFC patterns for regions rPC and lPCUN are shown in Figure 3B. All regional correlations were rank-ordered and are shown in Figure S5A. Regions located along in the posterior medial cortex (e.g the cuneus, precuneus and pericalcarine cortex in both hemispheres) are among those with the strongest SC-rsFC relationship at low resolution. We asked if the strength of the SC-rsFC relationship was related to network parameters. We detected weak but significant positive correlations between the number and strength of a region's anatomical connections, and the strength of the SC-rsFC correlation for that region.

These results remain preliminary because of two potential confounds. The first potential confound is the location of ROIs within the cerebral cortex. Because the cortical location of an ROI determines its distance to other regions of the brain, and inter-regional distance is known to effect SC and rsFC, as well as the accuracy of tractography algorithms, regional location can affect the SC-rsFC relationship. Secondly, the reliability of the automatic landmark-based registration algorithm differs across the brain. ROIs that can be more consistently localized across scans will tend to exhibit more reliable SC-rsFC relationships.

**Reliability of rsFC Measurement**

Because of the numerous potential sources – some physiological and some non-physiological – of variability in BOLD signal, it is difficult to be definitive regarding the origin of any observed rsFC measurement variability. Below we present some observations regarding this complex issue.

When we separately examined the reliability of rsFC for structurally connected versus unconnected edges, we found that structurally connected edges had more reliable rsFC, both in average data ($r=0.90$ versus $r=0.75$) and in each individual (Fig. S4). These effects could not be accounted for by the increased average proximity of structurally connected edges (surrogate data analysis not shown).

The increased reliability of rsFC among SC-present edges was also observed when comparing rsFC from the first 10 minutes against rsFC from the second 10 minutes within a single scanning session. The empirical rsFC reliability across 10 minute windows for SC-present edges is $r=0.66 \pm 0.08$, and for edges without SC the reliability is $r=0.47 \pm 0.08$. (These reliability values represent the mean and standard deviation across 5 participants.)

When comparing across consecutive 8-minute windows of simulated BOLD from our computational model, we found that for ROI pairs linked by SC, the mean inter-window correlations in rsFC was $r=0.75\pm0.04$, and for ROI pairs without SC it was $r=0.69\pm0.05$. (These reliability values represent the mean and standard deviation across 5 simulation runs, with each simulation employing the SC map of an individual participant.)

For all calculations of rsFC between two ROIs, at least 200 data points are employed. Based on numerical tests in which we (a) generated correlated time series, (b) measured the correlation between them, and then (c) re-sampled and re-measured the correlations while keeping the underlying interaction strengths constant, we conclude that both the model and the empirical data exhibit more variability in rsFC than can be attributed simply to sample size effects. Both the model and data exhibit unexpectedly low reliability, but the reliability is still lower in empirical data than in the model, most likely due to MRI acquisition and registration influences.

One of the characteristics shared in the model and the data is the presence of long-range temporal autocorrelation (which is sometimes called "long memory", and is also related to the presence of substantial power below 0.01 Hz in BOLD signal). In practice it can be impossible to distinguish long memory effects from intermittent changes in the underlying generating mechanisms of a time series [3], and long memory can also arise from the aggregation of numerous simple dynamical processes [4]. Alternatively, power in low frequencies may also arise from physiological sources [2]. We are not in a position to distinguish which combination of these effects we may be observing within our empirical measurements of BOLD signal, but in the model we can rule out physiological and MRI acquisition effects.

The difference in rsFC reliability between those ROI pairs with SC and those without SC may reflect the fact that SC facilitates a more persistent interaction between those ROIs. Alternatively, it may reflect the fact that SC-linked ROIs, for some other reason, have a stronger overall interaction which is then necessarily less variable under repeated finite-sample measurements. In either case, however, researchers can expect to observe more reliable rsFC measurements between ROI pairs that are anatomically linked.

Another consequence of this observation of diminished reliability is that, in quantifying the relationship between empirical SC and rsFC, we must keep in mind that SC can only predict rsFC to the extent that rsFC is constant. In participant B, for example, we observe that 27% of variance in rsFC within the first scan is explained in a bivariate regression using SC and fiber distance. To put this number in context, we observe that only 47% of the variance in rsFC in the second 10-minute window within that same scan is predicted by the rsFC observed in the first 10-minute window. So, SC and fiber distance together may have even more of a role in shaping rsFC than is suggested by the proportion of rsFC variance that they explain.

## Computational Models

In the main text we report results using a nonlinear model that produces simulated BOLD time series, but for comparison we also implemented a linear model for which the correlation structure in spontaneous dynamics can be calculated analytically [7]. More information concerning both the linear and nonlinear models are provided below, along with a brief comparison of the prediction performance of the linear and nonlinear models.

*Model Performance Comparison*. The correlation between simulated rsFC and empirical rsFC at direct links in the high resolution network was slightly higher in the linear than the nonlinear model (r=0.55 and r=0.46 respectively), while the nonlinear model yielded a better prediction of the rsFC between indirectly connected nodes (r=0.37 for the nonlinear versus r=0.26 for the linear model). In the low resolution networks, the correlation for both linear and nonlinear models between simulated and empirical rsFC increased to r=0.70 for directly linked pairs. Indirectly linked pairs were again better captured in the nonlinear model (r=0.23, versus r= −0.03 for the linear model).

*Linear Model*. The linear model we employed – a small variation on the model of Galán [5] -- is derived from the linearization around a fixed point of a general coupled neural system driven by spatially and temporally independent Gaussian noise sources. Within this framework, the correlation structure of the dynamics can be computed analytically given only the coupling matrix and a single parameter governing the rate of activation leakage from each node.

The model of Galán was derived by linearizing and discretizing the dynamics of a general Wilson-Cowan system. The discretized dynamics are governed by

$$\boldsymbol{u}(t+\Delta t) = A\boldsymbol{u}(t) + \xi(t)$$

where $\boldsymbol{u}$ is a vector of regional states, $\xi$ is a temporally white Gaussian noise term and $\Delta t$ is a time step. The generalized coupling matrix $A$ is defined as

$$A = (1-\alpha\Delta t)I + C\Delta t$$

where α is a leak variable from the activity within each node, $I$ is the identity matrix and $C$ is a matrix describing inter-nodal interaction efficacies. In place of $C$, we employed the resampled fiber strengths obtained from diffusion spectrum imaging tractography. Because this matrix contains only positive terms, the leak term α is chosen to be relatively large (α = 2), in order to retain a balance of driving and damping in the model.

Within this model, the covariance and correlation matrices of the nodal dynamics can be calculated analytically as a function of the eigenvalues of the matrix $A$, and of the covariance of noise terms input to each node. See reference [5] for further details.

*Nonlinear model*. The nonlinear model, as developed in [6] and extended to large-scale network settings in [7], is a neural mass model based on [8]. Each neural mass represents a local ensemble of neurons. The dynamical variables incorporated are the mean membrane potential of pyramidal cells, $V$, and inhibitory interneurons, $Z$, and the average number of 'open' potassium ion channels, $W$. The mean cell membrane potential of the pyramidal cells is governed by the conductance of sodium, potassium and calcium ion through voltage- and ligand-gated membrane channels,

$$\frac{dV}{dt} = -\left(g_{Ca} + r_{NMDA} a_{ee} Q_V\right) m_{Ca}\left(V - V_{Ca}\right) - \left(g_{na} m_{na} + a_{ee} Q_V\right)\left(V - V_{na}\right) - g_K W\left(V - V_K\right) - g_L\left(V - V_L\right) + a_{ie} Z Q_Z + a_{ne} I_\delta, \quad (1)$$

$$\frac{dZ}{dt} = b\left(a_{ni} I_\delta + a_{ei} V Q_V\right),$$

where $g_{ion}$ is the maximum conductance of each population of ion species if all channels are open, $m_{ion}$ is the fraction of channels open, $V_{ion}$ is the Nernst potential for that ion species and $Q_{V(Z)}$ is the firing rate of the excitatory (inhibitory) neurons. The fraction of open ion channels is determined by the sigmoid-shaped 'neural activation function',

$$m_{ion} = 0.5\left(1 + \tanh\left(\frac{V - V_T}{\delta_{ion}}\right)\right),$$

where $\delta_{ion}$ incorporates the variance of this distribution. The fraction of open potassium channels is governed by $W$, with

$$\frac{dW}{dt} = \frac{\phi\left(m_k - W\right)}{\tau},$$

where $\phi$ is a temperature scaling factor and $\tau$ is a 'relaxation' time constant. Cell firing rate is also determined by sigmoid activation functions,

$$Q_V = 0.5 x Q_{V\max}\left(1 + \tanh\left(\frac{V - V_T}{\delta_V}\right)\right),$$

where the $Q_{max}$ are the maximum firing rate. An analogous term is also introduced for the inhibitory cells.

The firing of excitatory and inhibitory cell populations feeds back onto the ensemble through synaptic coupling to open ligand-gated channels and raises or lowers the mean membrane potential accordingly. In the case of excitatory-to-inhibitory and inhibitory-to-excitatory connections, this is modeled as additional input to the flow of ions across the membrane channel, weighted by functional synaptic factors, $a_{ei}$ and $a_{ie}$. In the case of excitatory to excitatory connections, the rate of firing $Q_v$ is assumed to lead to a proportional release of glutamate neurotransmitter across the synapse, onto two classes of

ligand-gated ion channels: (1) AMPA channels, which open an additional population of sodium channels, and (2) NMDA receptors, which open an additional population of *voltage-gated* sodium and calcium channels. $r_{NMDA}$ incorporates the ratio of NMDA to AMPA receptors.

The equations above govern the dynamics within each local cell assembly. Coupling between $N$ nodes is introduced as competitive agonist excitatory action at the same populations of NMDA and AMPA receptors. Locating the $i$-th node at position $\mathrm{x}_i$ this is incorporated by modifying equation (1) to

$$\begin{aligned}\frac{dV(\mathbf{x}_i)}{dt} = &-\left(g_{Ca} + (1-c)r_{NMDA}a_{ee}Q_V(\mathbf{x}_i) + cr_{NMDA}a_{ee} < Q_V(\mathbf{x}) > \right) m_{Ca}\left(V(\mathbf{x}_i) - V_{Ca}\right) - g_K W\left(V(\mathbf{x}_i) - V_K\right) \\ &- g_L\left(V(\mathbf{x}_i) - V_L\right) - \left(g_{na}m_{na} + (1-c)a_{ee}Q_V(\mathbf{x}_i) + ca_{ee} < Q_V(\mathbf{x}) > \right)\left(V(\mathbf{x}_i) - V_{na}\right) \\ &+ a_{ie}ZQ_Z(\mathbf{x}_i) + a_{ne}I_\delta,\end{aligned}$$

for $i,j=1,\ldots,N$.

The parameter $c$ controls the strength of excitatory coupling between cortical regions. If $c=0$ the neural masses evolve independently. The setting $c>0$ introduces interdependences between linked regions, and $c=1$ corresponds to maximum coupling, with excitatory input from outside each region surpassing excitatory input from within each region. For the present paper, we chose a value for the excitatory coupling between regions of $c=0.15$, as this seemed to induce a reasonable balance of transient synchronization and desynchronization between regions. This value for the coupling parameter was set slightly higher than in ref [7] to adjust for the larger size and greater number of connections per node in the present model (runs with $c=0.10$ produced similar results but with overall lower cross-correlations). No attempt was made to model realistic conduction delays. All physiologically measurable parameters (conductances, threshold potentials and Nernst potentials) are set to values taken from [8]. The nonlinear model is simulated in Matlab R2007a (Mathworks, Natick, MA) at a time resolution of 0.2 msec. Before data analysis, resulting data sets are downsampled to a time resolution of 1 time step = 1 millisecond. After an initial transient of 2 minutes which was discarded, runs proceeded for a total of 16 minutes (960,000 msecs, $4.8 \times 10^6$ iterations). We ran four simulations with random initial conditions for each of the six structural connectivity matrices derived by DSI (two repeat scans for participant A, one scan for participants B-E).

To estimate BOLD signals for each neural mass, we followed [9] in employing a Balloon–Windkessel hemodynamic model [10,11]. Equations and parameters relating neuronal activity and vasodilatory signal with blood inflow, volume, and deoxyhaemoglobin content are taken directly from [8]. As in [7], the main input to the Balloon-Windkessel model, ‘‘neuronal activity,’’ is taken to be the absolute value of the

time derivative of the mean excitatory membrane potential within each brain region (i.e. a proxy for glutamate turnover). As in the empirical data, we detrended the data and regressed a global mean signal from each node's time series before calculating simulated rsFC maps. Unlike the empirical BOLD signals, there was not a very strong influence of a coherent global signal observed within the simulated BOLD before pre-processing.

The model performance results reported in Figure 1 and in Table S1 are for individual runs. Unless otherwise stated, the remainder of the model results is based on rsFC maps that are an average of four separate model runs.

Examination of fast voltage-time traces revealed complex synchronization dynamics as previously described in ref [7]. While in the current study we did not attempt to compute information flow patterns at high temporal resolution, the model does in principle allow for an investigation of synchrony and coherence at fast time scales.

**Structural and Functional Connectivity within the Default Mode Network**

The default mode network is reliably and robustly detected in resting state fMRI. We asked if the prominence of the Default Mode Network (DMN) in resting state activity can be accounted for by its structural connectivity. After extracting the 200 most strongly coupled ROIs comprising the DMN (see Fig. S5D) we determined the structural connection density within this network as well as the density of connections between the DMN and the 200 most anti-correlated ROIs. Within-DMN connection density was found to exceed the connection density between DMN and anti-correlated ROIs by more than 8-fold (0.074 versus 0.009, respectively). We then asked how the intra-DMN connection density compared relative to other networks that are extracted from 6 nonoverlapping clusters of seed ROIs symmetrically distributed across the two cerebral hemispheres. We formed a distribution of connection densities by randomly sampling 20,000 such networks. The DMN network is found to be in the top 1% of this distribution which has a mean of 0.050 and a standard deviation of 0.009. This indicates that the DMN represents a very highly and densely connected subnetwork within cortex.

The relationship between SC and rsFC was stronger within the DMN than across the entire cerebral cortex. For the 200 ROIs comprising the DMN, the presence of a structural connection predicted rsFC with $r = 0.64$, while the overall correlation between SC and rsFC was found to be $r = 0.55$. Both values greatly exceed those reported here for the entire cortex (see Table S1, 998 ROI data).

While both of our computational models accurately captured functional connectivity within the DMN along the medial wall of the cerebral cortex (Fig. 3C), they failed to account for the functional linkage of the lateral parietal cortex. An examination of the structural connection within the DMN (Fig. 3D) reveals that very few structural connections were detected between the precuneus/posterior cingulate cortex and the

lateral parietal cortex. The discrepancy between structural and functional connectivity in this portion of the DMN may be due to i) a failure of DSI to detect actually present structural connections, especially when tracking small fibers perpendicular to major fasciculi as in this case; ii) disproportionate physiological strengths within the DMN that compensate for the lack of strong structural coupling; iii) a significant role of other brain regions, not captured in the structural scans (e.g. the thalamus), in functionally linking lateral parietal cortex with the DMN.

These results were obtained using seed clusters for the default mode network derived from data reported in [12]. Similar result were found for slightly different sets of peak foci reported in [13,14].

**Supporting References**


[1] Aguirre GK, Zarahn E, D'Esposito M (1998) The inferential impact of global signal covariates in functional neuroimaging analyses. Neuroimage 8:302-6

[2] Shmueli K et al. (2007) Low-frequency fluctuations in the cardiac rate as a source of variance in the resting-state fMRI BOLD signal. Neuroimage. 38:306-20

[3] Diebold FX, Inoue A (2001) Long memory and regime switching. J Econometrics 105:131-159

[4] Granger CWJ (1980) Long memory relationships and the aggregation of dynamic models. J Econometrics 14:227-238

[5] Galán RF (2008) On how network architecture determines the dominant patterns of spontaneous neural activity. PLoS ONE 3:e2148

[6] Breakspear, M., Terry, J., Friston, K. (2003) Modulation of excitatory synaptic coupling facilitates synchronization and complex dynamics in a biophysical model of neuronal dynamics. Network: Computation in Neural Systems 14:703–732

[7] Honey CJ, Kötter R, Breakspear M, Sporns O (2007) Network structure of cerebral cortex shapes functional connectivity on multiple time scales. Proc Natl Acad Sci USA. 104:10240-5

[8] Larter R, Speelman B, Worth RM (1999) A coupled ordinary differential equation lattice model for the simulation of epileptic seizures. Chaos 9:795–804.

[9] Friston KJ, Harrison L, Penny W (2003) Dynamic causal modelling. NeuroImage 19:1273–1302.

[10] Mandeville JB et al. (1999) Evidence of a cerebrovascular postarteriole windkessel with delayed compliance. J Cereb Blood Flow Metab 19:679–689.

[11] Buxton RB, Wong EC, Frank LR (1998) Dynamics of blood flow and oxygenation changes during brain activation: the balloon model. Magn Reson Med 39:855–864.

[12] Fox MD et al (2005) The human brain is intrinsically organized into dynamic, anticorrelated functional networks. Proc Natl Acad Sci USA. 102:9673-8

[13] Greicius MD, Krasnow B, Reiss AL, Menon V (2003) Functional connectivity in the resting brain: a network analysis of the default mode hypothesis. Proc Natl Acad Sci USA. 100:253-8

[14] Mantini D, Perrucci MG, Del Gratta C, Romani GL, Corbetta M (2007) Electrophysiological signatures of resting state networks in the human brain. Proc Natl Acad Sci U S A. 104:13170-5.

# Supporting Information

**Honey *et al.* 10.1073/pnas.0811168106**

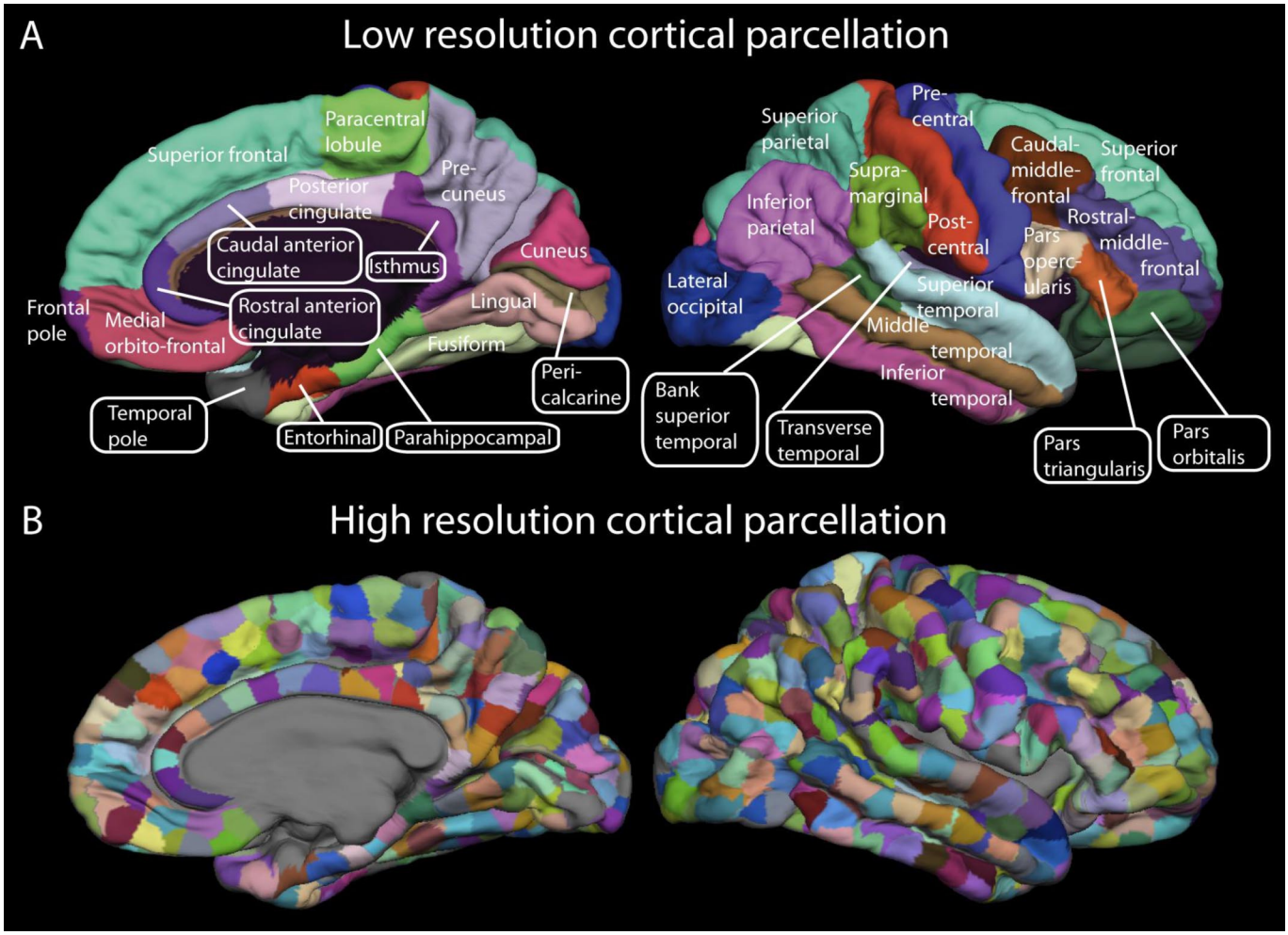


**Fig. S1.** (*A*) Low-resolution (66-region) and (*B*) high-resolution parcellations (998-ROI) of the cerebral cortex. In the article, the 66 cortical regions are labeled as follows: each label consists of two parts, a prefix for the cortical hemisphere (*r*, right hemisphere, *l*, left hemisphere) and 1 of 33 designators. BSTS, bank of the superior temporal sulcus; CAC, caudal anterior cingulate cortex; CMF, caudal middle frontal cortex; CUN, cuneus; ENT, entorhinal cortex; FP, frontal pole; FUS; fusiform gyrus; IP, inferior parietal cortex; IT, inferior temporal cortex; ISTC, isthmus of the cingulate cortex; LOCC, lateral occipital cortex; LOF, lateral orbitofrontal cortex; LING, lingual gyrus; MOF, medial orbitofrontal cortex; MT, middle temporal cortex; PARC, paracentral lobule; PARH, parahippocampal cortex; POPE, pars opercularis; PORB, pars orbitalis; PTRI, pars triangularis; PCAL, pericalcarine cortex; PSTS, postcentral gyrus; PC, posterior cingulate cortex; PREC, precentral gyrus; PCUN, precuneus; RAC, rostral anterior cingulate cortex; RMF, rostral middle frontal cortex; SF, superior frontal cortex; SP, superior parietal cortex; ST, superior temporal cortex; SMAR, supramarginal gyrus; TP, temporal pole; TT, transverse temporal cortex.

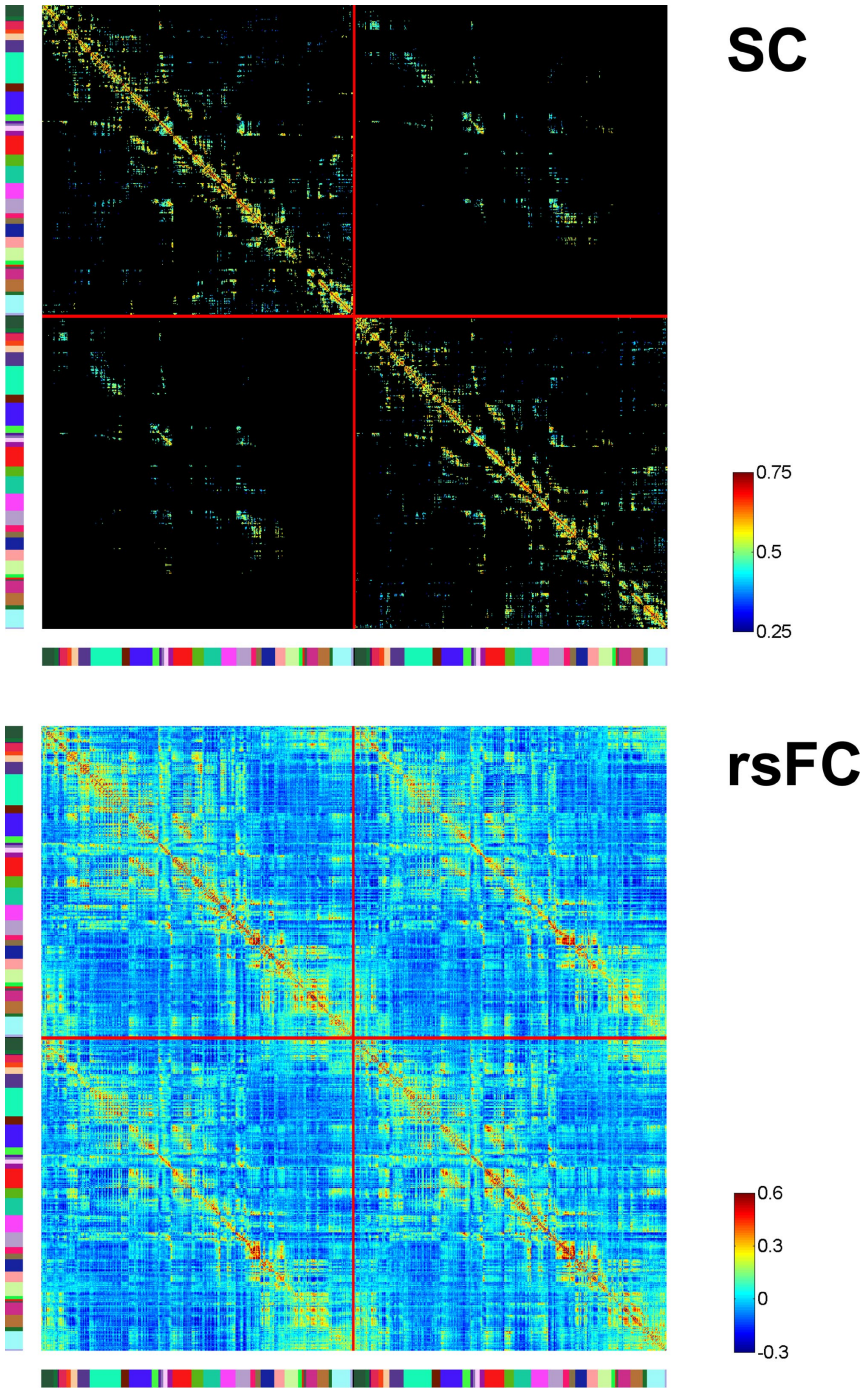


**Fig. S2.** Matrices of SC and empirical rsFC at the high resolution. Both plots represent averages across all 5 participants, including 2 structural scans for participant A, and 2 repeat functional scans for all 5 participants. The structural connection matrix is averaged after connection strengths were resampled to a Gaussian distribution with a mean of 0.5 and a standard deviation of 0.1. Connections that were present in only 1 out of 5 participants were set to zero strength. The functional connection matrix was computed from BOLD time series obtained for each ROI (see *Methods*). Each correlation value represents an average over 5 participants and 2 repeat scans per participant. The color bars at the left and bottom of the matrices indicate brain regions shown in a corresponding color map in Fig. S1.

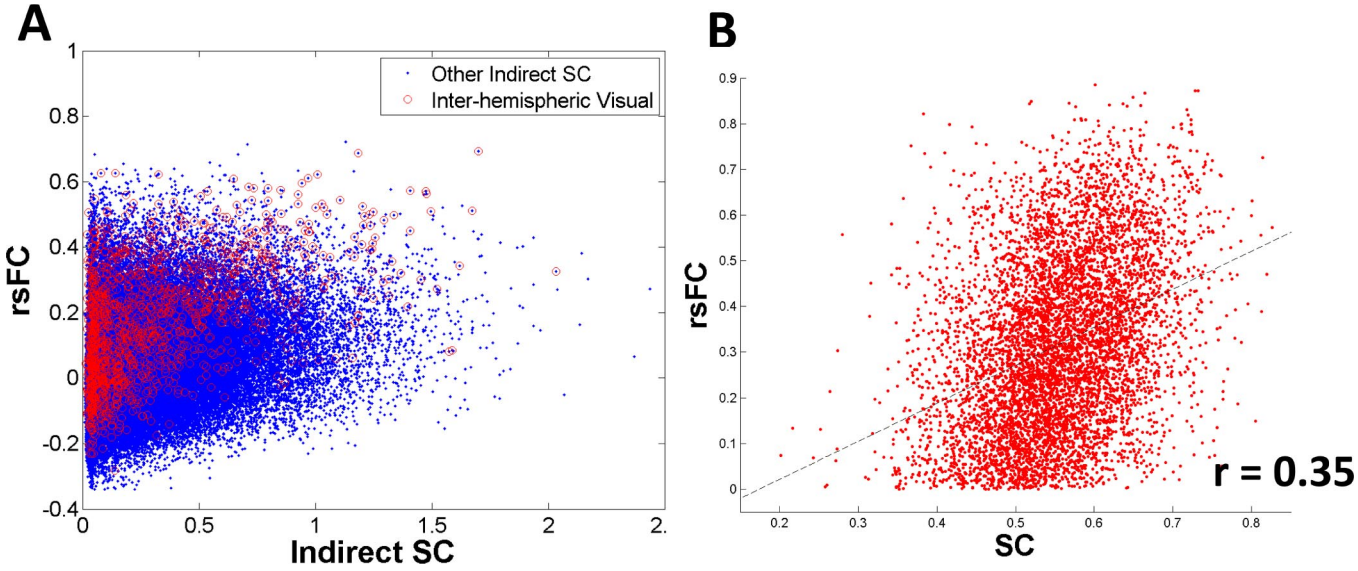


**Fig. S3.** (*A*) Indirect SC weakly predicts rsFC. The figure shows rsFC plotted against indirect SC (see *Results*) in the average high-resolution data. Plotted are those region pairs linked by at least one of the shortest paths of exactly 2 edges. Highlighted in red are the data points showing indirect SC and rsFC between the visual cortices in left and right hemispheres. Visual cortex ROIs within each hemisphere are those located in pericalcarine cortex, lateral occipital cortex, lingual gyrus, and the cuneus. (*B*) The SC-rsFC relationship for a single session from Participant A, at high resolution (998 ROIs), excluding all ROI pairs that exhibit anticorrelation. The SC-rsFC relationship does not depend on the presence of anticorrelations, nor on regression of a global mean BOLD signal.

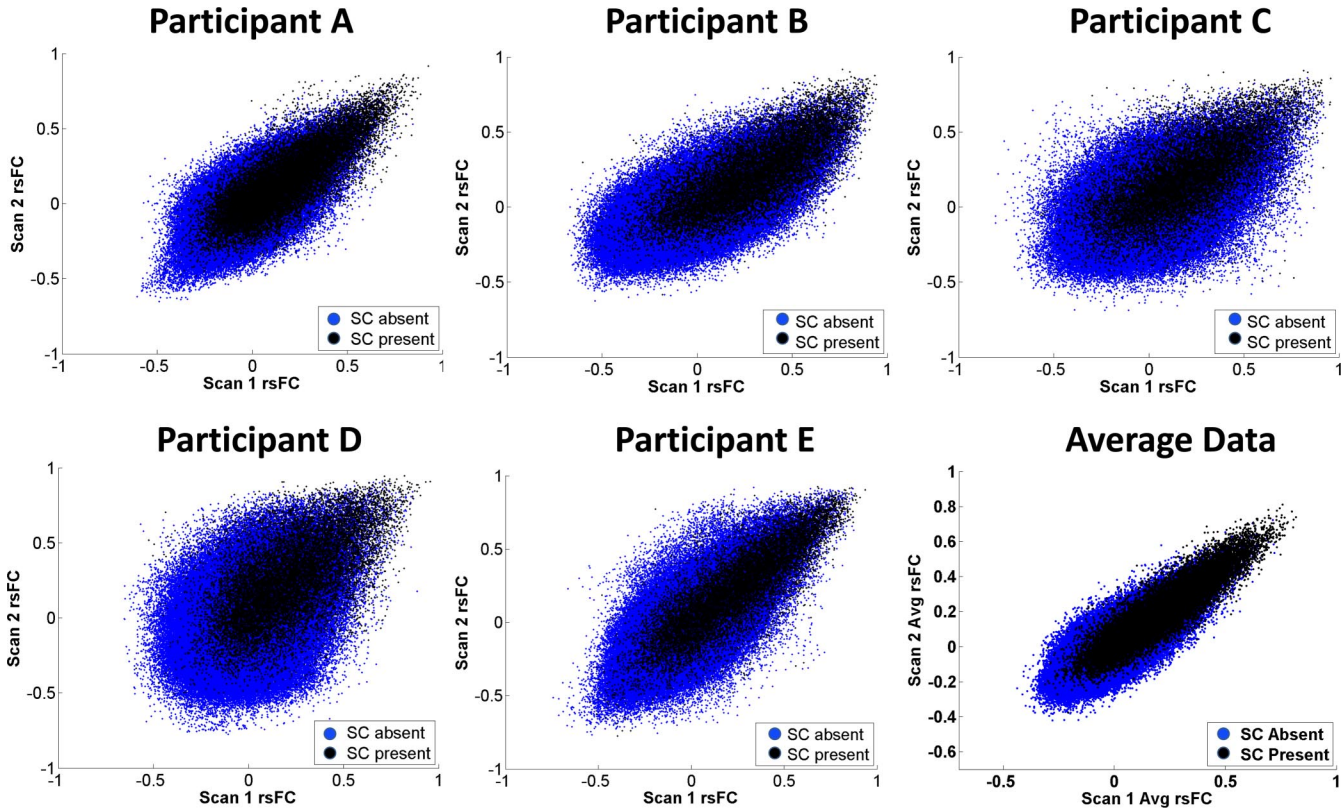


**Fig. S4.** Increased reliability of rsFC mediated by SC. The scatter plot shows rsFC from Scan 1 against rsFC from Scan 2, using high-resolution data for each of the 5 participants, as well as for participant-averaged SC and rsFC maps. Region-pairs with present SC in black, region-pairs without SC in blue.

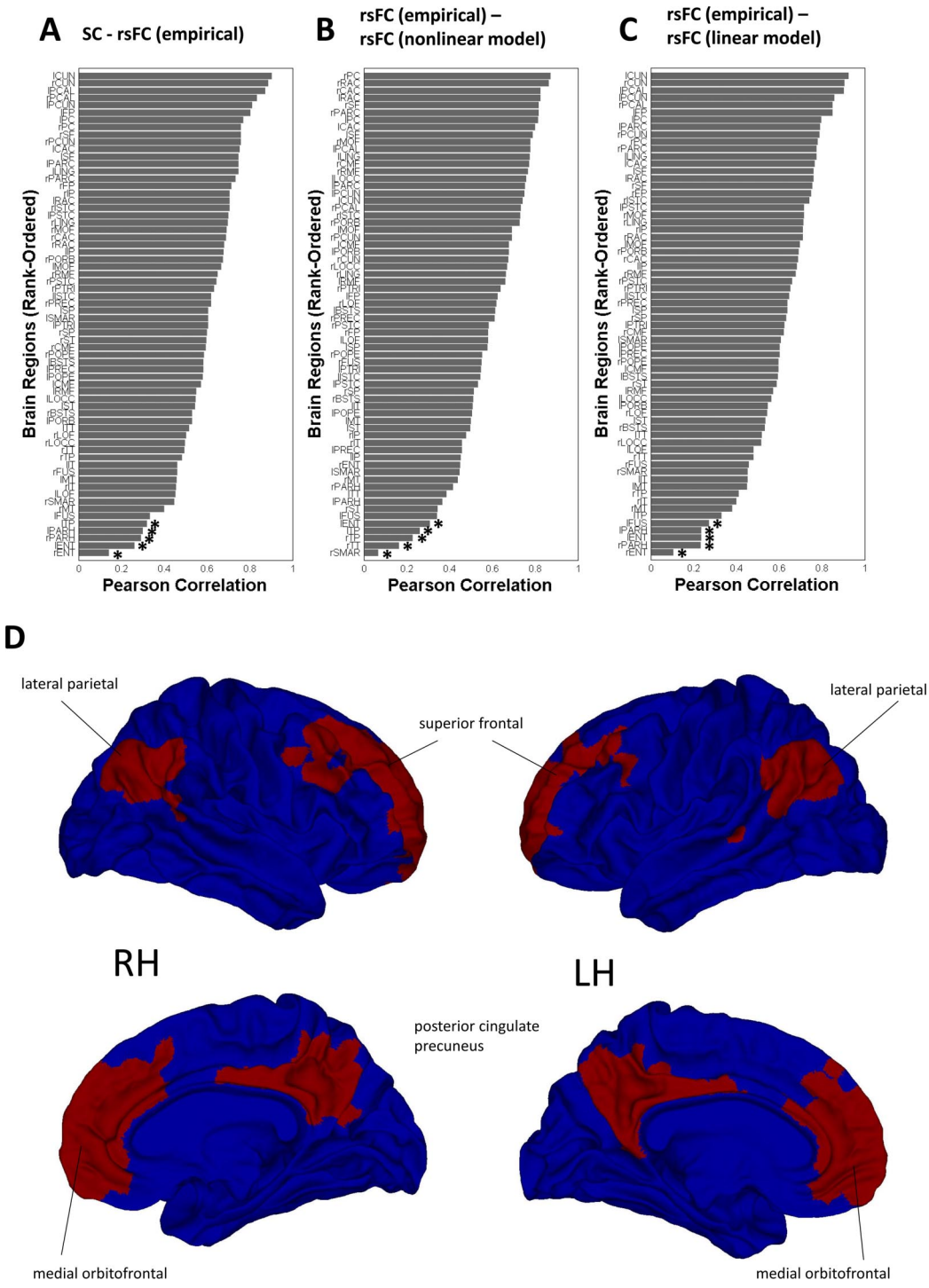


**Fig. S5.** Rank-ordered distribution of the strength of the relationships between structural connectivity, empirical functional connectivity, and simulated functional connectivity for single brain areas. Data were obtained at the low resolution from SC and rsFC matrices averaged over all 5 participants. (*A*) Pearson correlations for SC versus empirical FC. (*B*) Pearson correlations for empirical FC versus modeled FC (nonlinear model). (*C*) Pearson correlations for empirical FC versus modeled FC (linear model). All correlations except those marked with an asterisk are $P < 0.01$. (*D*) Seed ROIs used for extraction of the DMN shown in Fig. 3. These ROIs were determined as follows. We used published Talairach coordinates for 3 peak foci of task-negative network published by Fox *et al.* (12). These coordinates were (–2, –36, 37) in the posterior cingulate/precuneus [we added a symmetric coordinate at (2, –36, 37)], (–3, 39, –2) and (1, 54, 21) in the medial prefrontal cortex, and (–47, –67, 36) and (53, –67, 36) in the lateral parietal cortex. We identified clusters of 5 ROIs that were closest to each of these 6 target coordinates, resulting in a set of 30 ROIs. These 30 ROIs were used to compute the SC and rsFC maps shown in Fig. 3*C*. Given the empirical rsFC map, we then thresholded this map to obtain a set of 200 ROIs that were most strongly correlated (shown here in dark brown). This set of 200 ROIs covered most of the default-mode network and was used to display the structural connectivity linking these 200 ROIs in Fig. 3*D*.

**Table S1. Individual participant SC-rsFC and rsFC-distance correlations and corresponding values from individual runs of the computational model**

| Participant | Pearson Correlation with rsFC | | | | Model $R^2$ SC and fiber bivariate |
|---|---|---|---|---|---|
| | SC (All) | SC (Present) | Inverse fiber distance | Distance residuals | |
| 66 Regions | | | | | |
| A | 0.59 | 0.74 | 0.57 | 0.61 | 0.59 |
| B | 0.56 | 0.70 | 0.54 | 0.59 | 0.54 |
| C | 0.45 | 0.64 | 0.50 | 0.50 | 0.44 |
| D | 0.59 | 0.71 | 0.46 | 0.61 | 0.50 |
| E | 0.60 | 0.77 | 0.46 | 0.70 | 0.60 |
| Avg participant | 0.66 | 0.82 | 0.67 | 0.67 | 0.69 |
| 998 ROIs | | | | | |
| A | 0.24 | 0.42 | 0.39 | 0.24 | 0.20 |
| B | 0.24 | 0.48 | 0.47 | 0.23 | 0.27 |
| C | 0.18 | 0.39 | 0.40 | 0.18 | 0.19 |
| D | 0.23 | 0.42 | 0.40 | 0.23 | 0.20 |
| E | 0.22 | 0.42 | 0.39 | 0.24 | 0.21 |
| Avg participant | 0.36 | 0.53 | 0.47 | 0.30 | 0.30 |
| 998 Nodes | | | | | |
| A | 0.30 | 0.34 | 0.24 | 0.25 | 0.12 |
| B | 0.39 | 0.44 | 0.28 | 0.35 | 0.19 |
| C | 0.35 | 0.44 | 0.31 | 0.33 | 0.20 |
| D | 0.33 | 0.37 | 0.28 | 0.26 | 0.15 |
| E | 0.35 | 0.32 | 0.21 | 0.25 | 0.11 |
| Avg participant | 0.46 | 0.52 | 0.41 | 0.37 | 0.28 |

Individual participant SC-rsFC and rsFC-distance correlations (*Top* 2 sections), and corresponding values from individual runs of the computational model (*Bottom section*). Empirical rsFC is from the first fMRI scan; simulated rsFC is from a single 16 min simulation. The first 2 columns show the SC-rsFC correlations for ″all region pairs″ and for ″region pairs with SC,″ respectively. The third column shows the correlation between rsFC and the inverse of fiber distance, and the fourth column shows the correlation between SC and the residuals of the distance-regression. The fifth column provides the full model $R^2$ of a bivariate linear regression of rsFC on SC and inverse fiber distance. The bottom row shows the results of each calculation performed using data averaged across participants (it is not the average of the rows above). All correlations are $P << 1e\text{-}3$.

**Table S2. Interparticipant SC-rsFC correlations**

| | | Participant rsFC | | | | |
|---|---|---|---|---|---|---|
| All edges | | A | B | C | D | E |
| Participant SC | A | 0.237 | 0.211 | 0.164 | 0.205 | 0.197 |
| | B | 0.236 | 0.240 | 0.173 | 0.214 | 0.218 |
| | C | 0.232 | 0.224 | 0.180 | 0.215 | 0.204 |
| | D | 0.234 | 0.220 | 0.171 | 0.231 | 0.206 |
| | E | 0.222 | 0.212 | 0.165 | 0.210 | 0.225 |
| SC Present edges | | A | B | C | D | E |
| Participant SC | A | 0.415 | 0.407 | 0.329 | 0.379 | 0.383 |
| | B | 0.426 | 0.476 | 0.353 | 0.413 | 0.414 |
| | C | 0.450 | 0.461 | 0.392 | 0.422 | 0.424 |
| | D | 0.410 | 0.429 | 0.342 | 0.416 | 0.380 |
| | E | 0.379 | 0.409 | 0.345 | 0.385 | 0.424 |

The rsFC map is from the first fMRI scan.

**Table S3. Individual participant SC-rsFC and rsFC-distance correlations calculated without resampling of SC values**

| Participant | Pearson correlation with rsFC | | | | Model $R^2$ SC and fiber bivariate |
|---|---|---|---|---|---|
| | SC (All) | SC (Present) | Inverse fiber distance | Distance residuals | |
| 66 Regions | | | | | |
| A | 0.52 | 0.66 | 0.55 | 0.52 | 0.49 |
| B | 0.46 | 0.57 | 0.51 | 0.44 | 0.41 |
| C | 0.38 | 0.53 | 0.49 | 0.38 | 0.35 |
| D | 0.50 | 0.60 | 0.45 | 0.48 | 0.39 |
| E | 0.44 | 0.57 | 0.44 | 0.48 | 0.38 |
| Avg Participant | 0.58 | 0.71 | 0.66 | 0.50 | 0.57 |
| 998 ROIs | | | | | |
| A | 0.18 | 0.34 | 0.39 | 0.21 | 0.19 |
| B | 0.15 | 0.30 | 0.46 | 0.13 | 0.24 |
| C | 0.13 | 0.28 | 0.40 | 0.14 | 0.18 |
| D | 0.16 | 0.30 | 0.39 | 0.17 | 0.18 |
| E | 0.16 | 0.31 | 0.39 | 0.19 | 0.19 |
| Avg Participant | 0.30 | 0.46 | 0.47 | 0.27 | 0.28 |

rsFC is from the first fMRI scanning session. The SC strength is equal to the number of tractographic streamlines linking two ROIs, divided by the total area of the two ROIs. The first 2 columns show the SC-rsFC correlations for ″all region pairs″ and for ″region pairs with SC,″ respectively. The third column shows the correlation between rsFC and the inverse of fiber distance, and the fourth column shows the correlation between SC and the residuals of the distance-regression. The fifth column provides the full model $R^2$ of a bivariate linear regression of rsFC on SC and inverse fiber distance. The bottom row shows the results of each calculation performed using data averaged across participants (it is not the average of the rows above).

**Table S4. Individual participant SC-rsFC and rsFC-distance correlations, after rsFC maps are Fisher-z transformed and then normalized to zero mean and unit variance across the 998 ROIs of each participant**

| | Pearson correlation with rsFC | | | | Model $R^2$ SC and fiber bivariate |
|---|---|---|---|---|---|
| Participant | SC (All) | SC (Present) | Inverse fiber distance | Distance residuals | |
| 66 Regions | | | | | |
| A | 0.60 | 0.75 | 0.55 | 0.64 | 0.58 |
| B | 0.58 | 0.71 | 0.52 | 0.61 | 0.54 |
| C | 0.45 | 0.64 | 0.49 | 0.52 | 0.44 |
| D | 0.61 | 0.71 | 0.45 | 0.62 | 0.51 |
| E | 0.62 | 0.77 | 0.44 | 0.72 | 0.61 |
| Avg Participant | 0.68 | 0.82 | 0.66 | 0.68 | 0.69 |
| 998 ROIs | | | | | |
| A | 0.25 | 0.41 | 0.38 | 0.24 | 0.20 |
| B | 0.25 | 0.47 | 0.46 | 0.24 | 0.25 |
| C | 0.19 | 0.39 | 0.39 | 0.19 | 0.18 |
| D | 0.24 | 0.41 | 0.38 | 0.24 | 0.20 |
| E | 0.24 | 0.42 | 0.38 | 0.26 | 0.21 |
| Avg Participant | 0.38 | 0.53 | 0.46 | 0.32 | 0.30 |

The first 2 columns show the SC-rsFC correlations for ″all region pairs″ and for ″region pairs with SC,″ respectively. The third column shows the correlation between rsFC and the inverse of fiber distance, and the fourth column shows the correlation between SC and the residuals of the distance-regression. The fifth column provides the full model $R^2$ of a bivariate linear regression of rsFC on SC and inverse fiber distance. The bottom row shows the results of each calculation performed using data averaged across participants (it is not the average of the rows above).

## Other Supporting Information Files

*SI Appendix*